Design of Asymmetric Peptide Bilayer Membranes

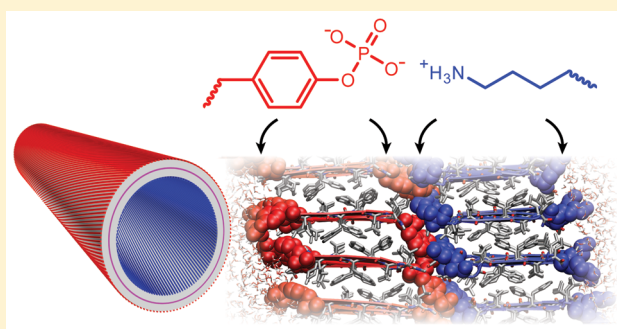Sha Li,[†] Anil K. Mehta,[*,‡] Anton N. Sidorov,[§] Thomas M. Orlando,[§,‖] Zhigang Jiang,[‖] Neil R. Anthony,[⊥] and David G. Lynn[*,†]

[†]Departments of Biology and Chemistry, [‡]Emory NMR Center, [⊥]Emory Integrated Cellular Imaging Core, Emory University, Atlanta, Georgia 30322, United States

[§]School of Chemistry and Biochemistry and [‖]School of Physics, Georgia Institute of Technology, Atlanta, Georgia 30332, United States

S Supporting Information

ABSTRACT: Energetic insights emerging from the structural characterization of peptide cross-β assemblies have enabled the design and construction of robust asymmetric bilayer peptide membranes. Two peptides differing only in their N-terminal residue, phosphotyrosine vs lysine, coassemble as stacks of antiparallel β-sheets with precisely patterned charged lattices stabilizing the bilayer leaflet interface. Either homogeneous or mixed leaflet composition is possible, and both create nanotubes with dense negative external and positive internal solvent exposed surfaces. Cross-seeding peptide solutions with a preassembled peptide nanotube seed leads to domains of different leaflet architecture within single nanotubes. Architectural control over these cross-β assemblies, both across the bilayer membrane and along the nanotube length, provides access to highly ordered asymmetric membranes for the further construction of functional mesoscale assemblies.

INTRODUCTION

Amphiphiles ranging from synthetic detergents to more complex biological phospholipids often assemble as symmetric membrane bilayers. More recently amphiphilic peptides that assemble as fibers and hydrogels[1−5] have been shown to form bilayer membranes[6−8] maintaining the characteristic cross-β architecture of amyloid.[9,10] These assemblies can have β-sheets with antiparallel strands creating a bilayer leaflet interface composed of precisely patterned and charged strand termini[11,12] (Figure S1). This distinct structure offers insight into the design and construction of various ordered bilayer architectures, including self-assembling asymmetric bilayers.

Peptide cross-β bilayer membranes for both the positively charged Ac-KLVFFAL-NH$_2$ (K)[11] and the negatively charged Ac-(pY)LVFFAL-NH$_2$ (pY)[13] nanotubes are as thick as natural phospholipid membranes.[11,13] The β-strands are oriented perpendicular to the nanotube long axis as out-of-register antiparallel β-sheets with the N-terminal residues positioned outside the H-bonded β-sheet (Figure 1). Stacking of these β-sheets creates the leaflets of the peptide bilayer[8] with an internal interface consisting of the charged strand termini (Figure 1B,D and Figure S1G,H). The tension created by the packing[14] of these charged surfaces defines the helical pitch angle that controls nanotube diameter. Incorporation of carboxylate counterions of TFA[8] passivates the peptide leaflet interface for the K peptide nanotubes, while TEA ions[13] stabilizes the negatively charged pY peptide lattice association (Figure 1B,D).

To the extent that charge neutralization at the peptide leaflet interface stabilizes bilayer assembly, the coassembly of oppositely charged K and pY peptides should result in self-passivating assemblies. Of the range of possible outcomes, the two limiting models of heterogeneous (Figure 2A) and homogeneous leaflets (Figure 2B) could each achieve interfacial charge compensation at the leaflet interface. Both cases would result in global bilayer surface charge asymmetry with oppositely charged surfaces (Figure 2C,D). Here we show that coassembly of the K and pY peptides indeed form robust nanotubes maintaining global asymmetric bilayer architectures. We use detailed structural analyses, benefiting significantly from the characterizations of single peptide assemblies,[11,13,15] to create specific domains existing within the length of the bilayer nanotubes. The electrochemical potential and the "bamboo-like" domain architectures of these bilayers can now be functionally exploited as self-assembling asymmetric architectures geometrically compatible with biological membranes.
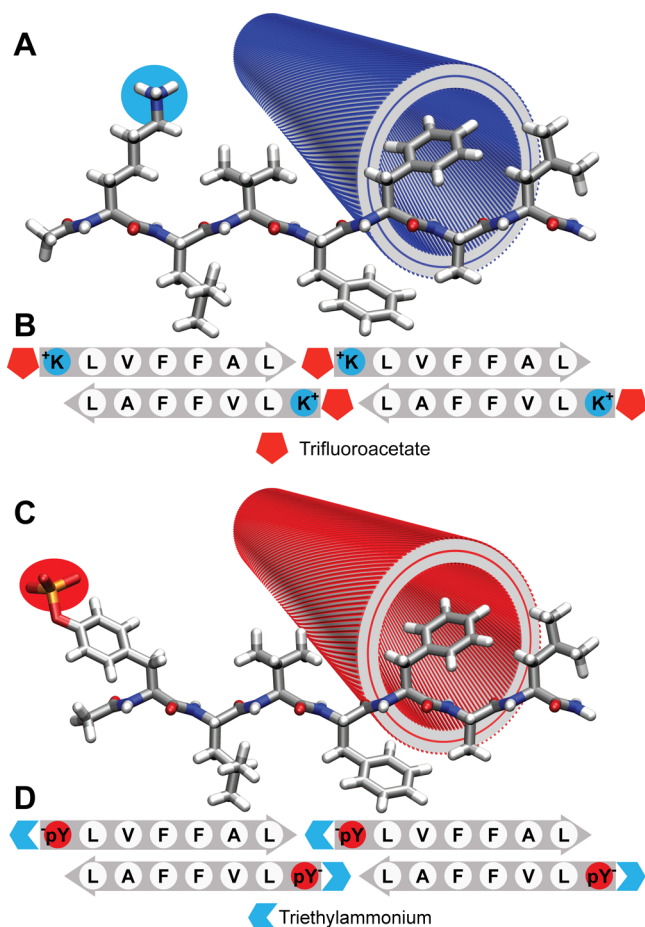
RESULTS AND DISCUSSION

**K/pY Peptides Coassemble As Robust Nanotubes.** When equimolar suspensions of preassembled K and pY peptide nanotubes are pelleted separately and then cosuspended in 40% MeCN/H$_2$O at neutral pH, the characteristic red-shifted β-sheet ellipticity at 225 nm for β-sheet rich

Figure 1. Models for Ac-KLVFFAL-NH$_2$ (K) and Ac-(pY)LVFFAL-NH$_2$ (pY) peptide bilayer nanotubes. Blue and red circles indicate positive and negatively charged N-terminal residues with blue (TEA, triethylammonium) and red (TFA, trifluoroacetate) polygon shapes corresponding to counterions. Both the K (A) and pY (C) peptides assemble as antiparallel, out-of-register register β-sheets (B and D) to give each leaflet of the nanotube bilayers.
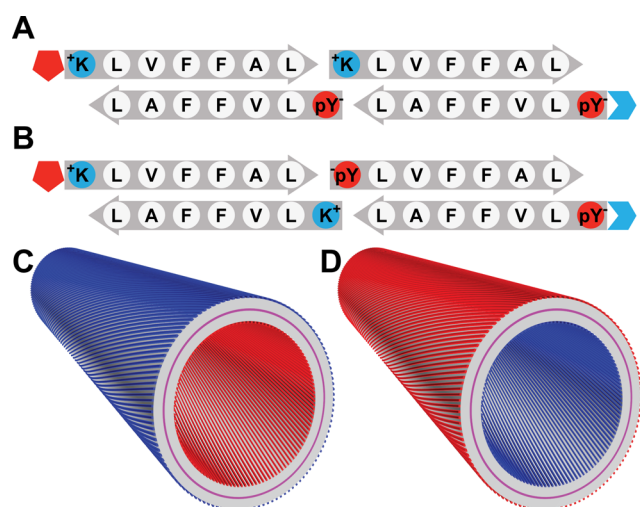
Figure 2. Models for coassembled peptide nanotubes. Blue and red represent positive and negative charges, respectively. Two β-sheet arrangements are possible to give (A) heterogeneous and (B) homogeneous leaflets. Each arrangement will generate segregated charged surfaces (C) and (D).

nanotubes[11,12,16] is lost immediately. In less than an hour, however, this β-sheet CD signature develops again and becomes more intense than observed for either of the initial pure K or pY nanotubes (Figure S2A). Mixing equimolar solutions of the K/pY peptides also leads to coassembly under the same 40% MeCN/H$_2$O conditions at neutral pH, but more than 3 days are required for measurable β-sheet ellipticity to be observed. After 3−6 weeks, this coassembly also achieves greater β-sheet ellipticity than either pure peptide assembly (Figure S2B). Morphologically, both conditions result in nanotubes similar to the individual peptide assemblies as visualized by TEM[8,11,16−18] (Figure 3A,D,G) with 53.1 nm
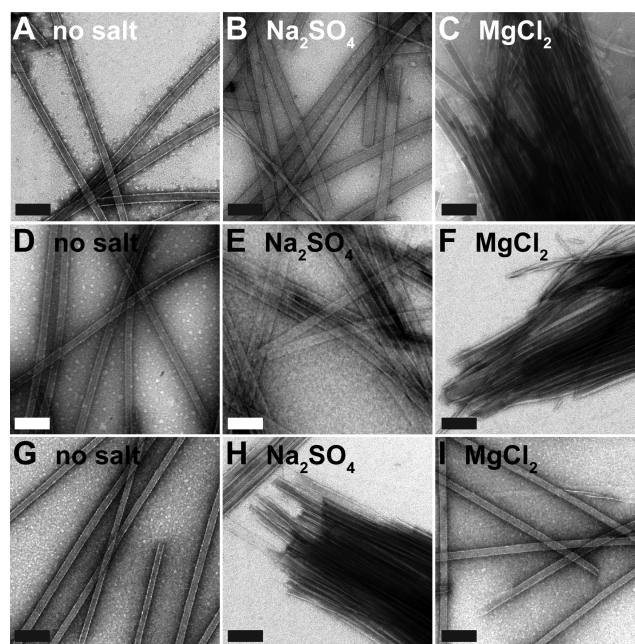

Figure 3. Transmission electron micrographs of salt-induced bundling. K/pY mixed peptides (top), pY (middle) and K peptide (bottom) nanotubes: (A, D and G) without additional salts, (B, E and H) 2 h after the addition of Na$_2$SO$_4$, and (C, F and I) 2 h after the addition of MgCl$_2$. Peptide/salt molar ratio of 1:4.5 and scale bars are 200 nm.

widths for a diameter 33.8 ± 0.8 nm (Figure S2C). Each nanotube also contains a strong amide-I IR stretch at 1623 cm^{-1} with a weaker band at 1693 cm^{-1} (Figure S2D), signatures typical of antiparallel β-sheets.[11,19−22] Powder X-ray diffraction (XRD) (Figure S2E) has reflections with d-spacings at 4.7 and 10.6 Å, characteristic of the orthogonal peptide spacing in β-strands and β-sheets, respectively, for cross-β assemblies.[9−11,23−26] Support for these coassemblies being stabilized by cooperative electrostatic interactions between oppositely charged peptides in adjacent leaflets (Figure 2A,B) is reflected in thermal melting analyses (Figure S3). In 40% MeCN, only the K peptide nanotubes melt (T_m) at 48.5 ± 15.6 °C (Figure S3, Table S1), while the pY peptide nanotubes and the mixed assemblies do not melt (Figure S3). Resuspending the mature nanotubes in higher organic:water solvents decreases the T_m of all the nanotubes (Table S1), where in 90% MeCN aqueous solutions, the pY nanotubes have a calculated T_m of 17.3 °C (Figure S4) while the coassembled K/pY nanotubes melt cooperatively at 52 ± 10.3 °C (Figure S3).

Coassembled K/pY Peptide Nanotubes Have Negatively Charged Surfaces. Our bilayer-leaflet charge

compensation model creates homogeneously charged outer and inner tube surfaces, but does not predict whether the K or the pY N-terminal residues localize to inner or outer surfaces. Salt-induced bundling of the K/pY coassemblies (Figure 3A−C) shows that only MgCl$_2$ and not Na$_2$SO$_4$ induces bundling, as visualized by TEM. As controls, only MgCl$_2$ bundles the negatively charged pY nanotubes and only Na$_2$SO$_4$ induces bundling of the positively charged K nanotubes, consistent with Hofmeister series counterion-induced aggregation[13,17] and indicates excess phosphate negative charge density on the outer surface of the K/pY peptide coassembled nanotubes.

To confirm peptide nanotube surface charge, enhanced-electrostatic force microscopy (EFM) maps charge distribution,[27−30] and Figure 4 contains the topographical and EFM
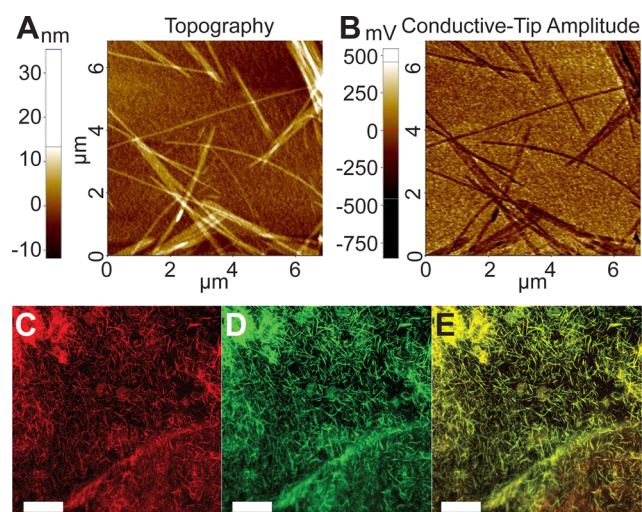

Figure 4. (A) Topography and (B) EFM amplitude micrographs of mature K/pY coassemblies in 40% MeCN/H$_2$O. EFM (DC bias of +1 V) shows positively charged surfaces as light and negatively charged surfaces as dark. Single slices of confocal fluorescence image of (C) Alexa 633 in the presence of K/pY coassembled nanotubes, (D) acridine orange in the presence of K/pY coassembled nanotubes, (E) overlay of images (C) and (D). Scale bar 40 μm.

amplitude images of the mature K/pY peptide coassemblies. At maturity, each detected assembly is homogeneously negative (dark) along its entire length, identical to the pY assemblies.[13] As early as 10 min after mixing the K and pY peptides, amorphous aggregates show positive, negative and neutral domains (Figure S5), but as seen for the individual peptide assemblies (Figure S6),[13] this heterogeneity resolves over the first 20 days to give assemblies where the outer surface is homogeneously negatively charged for at least 7 weeks.[13]

As shown in Figure 4C,D, confocal fluorescence identifies that both the negatively charged Alexa 633 and positively charged acridine orange dyes bind to the K/pY coassemblies. Consistent with electrostatic attraction/repulsion, negatively charged Alexa 633 binds to the K nanotubes and not to pY nanotubes while positively charged acridine orange binds specifically to pY not to K assemblies (Figure S7). The overlaid image (Figure 4E) finds that the majority of Alexa 633 and acridine orange are colocalized on the K/pY coassembly nanotubes, and when combined with the EFM and salt-bundling results, supports a model where the nanotubes maintain a negative external surface and a positive internal surface as depicted in Figure 2D. While the resolution of these

experiments is insufficient to quantify defects, there are regions where only single dyes appear bound (Figure 4E).

Coassembled K/pY Peptide Nanotubes Contain Both Leaflet Architectures. Constraining the K/pY nanotubes to negative outer (pY-rich) and positive inner (K-rich) surfaces (Figure 5A) facilitated the design of specific ^{13}C and ^{15}N
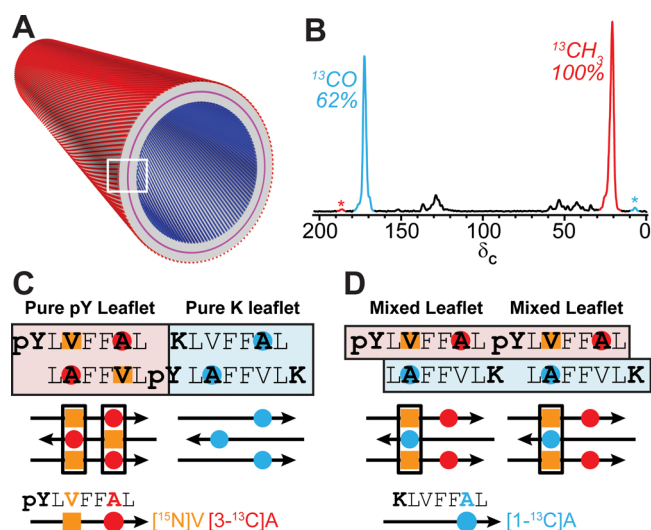

Figure 5. ^{13}C, ^{15}N peptide enrichment scheme to assess leaflets of K/pY peptide coassemblies. (B) Backbone [1-^{13}C] enrichment of Alanine in K peptides (blue circles) and methyl side chain [3-^{13}C] of Alanine in pY peptides (red circles) can be distinguished by ^{13}C chemical shifts. ^{13}C spectra indicate that assemblies consist of 0.62 K peptides for every pY peptide. Backbone [^{15}N] enrichment of pY peptide (orange squares) is utilized to distinguish between leaflets composed of (C) pure pY/pure K peptides from leaflets (D) containing both pY and K peptides.

peptide enrichment to define the leaflet composition by solid-state NMR as outlined in Figure 5. Assuming the peptide orientation within the K/pY coassembled nanotubes is identical to the pure pY[13] and pure K[11] nanotubes (Figure 1B,D) with antiparallel out-of-register β-strands, the alanine residues will be directly H-bonded to the valine residues (Figure 1B,D). As the ^{13}C NMR resonances of alanine side chain methyl [3-^{13}C] carbons and the backbone valine carbonyl [1-^{13}C] carbons are separated by ~150 ppm (Figure 5B), these residues were selected to provide specific signatures for the pY and K peptides, respectively. ^{13}C−^{15}N distance measurements provide a means to interrogate which peptide is directly H-bonded to ^{15}N enriched valine residues of the pY peptide (Figure 5C,D) by measuring ^{13}C−^{15}N dipolar couplings with ^{13}C{^{15}N}-REDOR (Rotational-Echo Double-Resonance) experiments.[31,32] Pure pY peptide leaflets (Figure 5C) will have the pY peptide [3-^{13}CH$_3$]Ala H-bonded to neighboring pY peptides [^{15}N]Val. In contrast, mixed pY/K peptide leaflets (Figure 5D) will have the K-peptide [1-^{13}C]Ala H-bonded to pY-peptides [^{15}N]Val.

When assembled in 40%MeCN/H$_2$O at neutral pH with equal starting K (Ac-KLVFF[1-^{13}C]AL-NH$_2$) and pY (Ac-(pY)L[^{15}N]VFF[3-^{13}C]AL-NH$_2$) peptide concentrations, the integrated alanine methyl ^{13}CH$_3$ and carbonyl ^{13}CO resonances in sedimented assemblies corresponds to a K/pY peptide ratio of 0.62 (Figure S8), suggesting that some of the heterogeneity in the fluorescent images arises from the excess pY peptide in the nanotube coassembly.

The alanine carbonyl chemical shift of 172.5 ppm for the Ac-KLVFF[1-^{13}C]AL-NH$_2$ (K) peptides is consistent with all of the K-peptides being in H-bonded β-sheets.[33] Experimental ^{13}C{^{15}N}REDOR data for the backbone alanine ^{13}CO indicates that a majority of the alanine residues of Ac-KLVFF[1-^{13}C]AL-NH$_2$ (K) peptides are H-bonded to a [^{15}N] of the valine pY peptides, but in contrast to the simple model of mixed leaflets (Figure 5D), the data are not accurately fit by simulations for a heterogeneous leaflet three-spin system for a ^{13}C surrounded by two ^{15}N atoms from neighboring β-strands (Figure 6, black
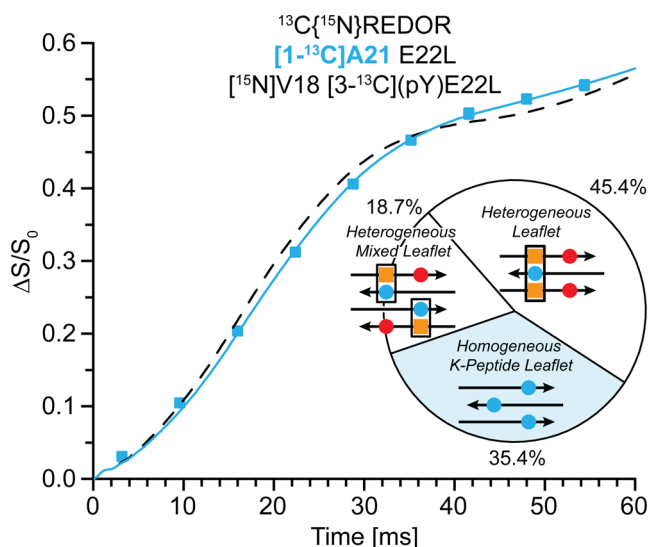
Figure 6. [1-^{13}C]Ala ^{13}C{^{15}N}REDOR dephasing of the Ac-KLVFF-[1-^{13}C]AL-NH$_2$ and Ac-(pY)L[^{15}N]VFF[3-^{13}C]AL-NH$_2$ coassemblies. [1-^{13}C]Ala ^{13}C{^{15}N}REDOR dephasing reports on K peptides that are H-bonded to the [^{15}N] alanine of the pY peptides within antiparallel β-sheets. Dashed black line is best fit assuming only a heterogeneous leaflet with K peptide H-bonded to two pY peptides, consistent with only 63% of K-peptides being close to ^{15}N. Best fit (blue line) requires three populations: 45.4% of K peptides surrounded by 2 pY peptides in a heterogeneous leaflet with ^{13}C−^{15}N distances of $r_1 = 4.32$ and $r_2 = 5.3$ Å and a ^{15}N−^{13}C−^{15}N internuclear angle of 155°, 18.7% of K peptides H-bonded to a single pY peptide in a heterogeneous mixed leaflet and the plateau of the experimental data indicates that 35.4% of the K peptide alanine ^{13}CO's are not close to an ^{15}N, consistent with a homogeneous leaflet of pure K peptide.

curve) as previously developed for such extended β-sheet arrays (Figure S9).[11,13,34] Moreover, the three-spin ^{13}C{^{15}N}REDOR curve plateau is consistent with only 63% of the K peptides being adjacent to two pY peptides and the remaining 37% not adjacent to any pY peptides. These data suggest the existence of an extended homogeneous all K-peptide block leaflet segment. While the simulated three-spin heterogeneous leaflet dephasing rate captures the general shape of experimental data, better fits were obtained by having a portion of the alanine ^{13}CO being H-bonded to only a single [^{15}N]pY peptide creating a two-spin ^{13}C−^{15}N ensemble with ^{13}C−^{15}N distances corresponding to one of the two ^{15}N distances. The best fit is obtained with the 3-spin contribution reduced to 45.4 ± 4.7% and the remaining 18.7 ± 5.4% assigned to 2-spin contributions (Figure 6, inset).

The presence of distinct domains is further supported by fits to ^{13}C{^{15}N}REDOR dephasing of the pY peptide side chain methyl ^{13}C carbon (Figure S10) in Ac-(pY)L[^{15}N]VFF[3-^{13}C]-AL-NH$_2$ as shown in Figure 7. Best fits place 27.0 ± 2.4% of the pY-peptides in the extended 3-spin arrangement, 46.3 ± 3.0%
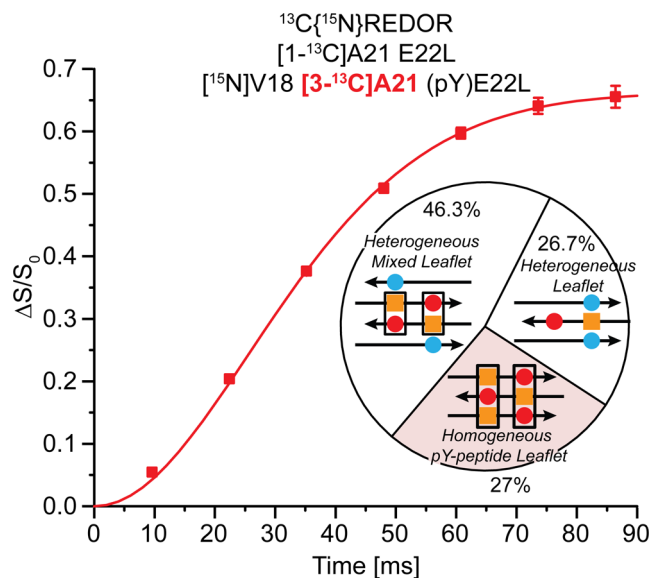

Figure 7. [3-^{13}C]Ala ^{13}C{^{15}N}REDOR dephasing of the Ac-KLVFF-[1-^{13}C]AL-NH$_2$ and Ac-(pY)L[^{15}N]VFF[3-^{13}C]AL-NH$_2$ peptide coassembly. Methyl carbon [3-^{13}C]Ala dephasing reports on pY peptides that are H-bonded to the [^{15}N]Ala of pY peptides within antiparallel β-sheets. The best fit (red line) requires three populations of pY peptides: 27% in a homogeneous pY leaflet with ^{13}C−^{15}N distances of $r_1 = 5.2$ Å and $r_2 = 5.3$ Å with a ^{15}N−^{13}C−^{15}N internuclear angle of 127° and two heterogeneous leaflets, 46.3% with pY peptides H-bonded to only a single pY and 26.7% where the [3-^{13}C]Ala is not proximal to any [^{15}N]Ala.

in 2-spin arrangements, and the remaining 26.7 ± 3.8% of the side chain methyl not being close to an ^{15}N. These determinations are consistent with 3-spin, ^{15}N−^{13}C−^{15}N, arrangements in homogeneous leaflets, 2-spin, ^{13}C−^{15}N, arrangements containing either 4.3 or 5.3 Å distances, and in heterogeneous leaflets with no dephasing (Figure 7, inset).

The proportion of K and pY peptides arranged in homogeneous leaflets can then be approximated as 35.4 ± 7.0% × 0.62 = 21.9 ± 4.4% and 27.0 ± 2.4%, respectively. To match the observed negatively charged outer surface of the nanotubes, 25% of the assemblies could contain homogeneous outer pY and inner K leaflets. The same approximation can be used for the heterogeneous leaflets, 45.4 ± 2.4% × 0.62 = 28.1 ± 2.9% and 26.7 ± 3.8%, respectively, for another quarter of the assemblies containing alternating K/pY peptide leaflets. The nonalternating repeats are dominated by the excess pY peptides in the assemblies, possibly at domain interface sites not resolved by EFM. Conformation of these assignments will require the development of precise cross-leaflet constraints.

K/pY Peptide Coassembly Can Generate Distinct Domains within Individual Nanotubes. The spectroscopic results do not unequivocally assign the resolved architectures to separate nanotubes or as coexisting within individual nanotubes. However, as shown in Figure 8A, uranyl acetate staining differentiates pY and K nanotube surfaces.[13] Sonication of mature K and pY nanotubes generates short segments with ends that might be used as templates for nanotube growth. The micrographs in Figure 8B arise from the use of the K nanotube seeds to initiate assembly of pY peptide solutions (Figure 8B), and correspondingly in Figure 8C, pY seeds to nucleate growth of K peptide solutions. In both cases, the seeding domains are resolved by staining, confirming that both K and pY nanotube assemblies template growth of the oppositely charged peptide.
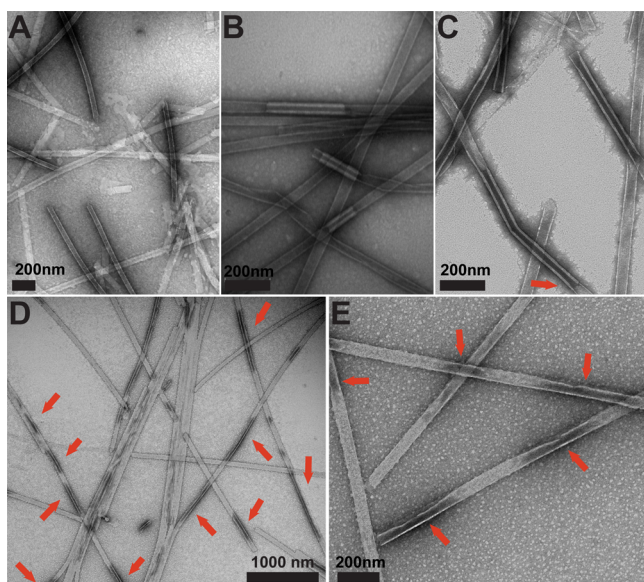
Figure 8. Transmission micrographs of seeded assemblies. (A) Separate K and (pY) assemblies placed sequentially on a same grid. Seeds are prepared for (B) (pY) solutions templated with K nanotube seeds, (C) K solutions templated with pY nanotube seeds, and (D) K solutions templated with K/(pY) coassembly seeds. Arrows highlight domains structures in (D) and (E) expansions of D.

The more stable and architecturally diverse seeds prepared from the K/pY coassembled nanotubes also induced K peptide assembly (Figure 8D, E). These assemblies show extensive segmentation along the length of individual tubes, generating structurally distinct domains that break the lateral symmetry of the nanotube architecture. Such "bamboo-like" architectures have been observed with fluorescence dynamics measurements[35] and implicated in conformational mutations during propagation,[36,37] and we suspect that control of such lateral asymmetry emerges from dynamic associations of seed templates with transitory particles of the K peptide, opening entirely new mesoscale design strategies to be further explored.

CONCLUSIONS

More than 40 years ago, the fluid mosaic model described phospholipid bilayers as a 2D liquid.[38] The remarkable fluidity and plasticity of such symmetric bilayers stabilized by hydrophobic leaflet interfaces are critical to all cellular life. However, that criticality is continually maintained at a significant energetic cost. Asymmetric leaflet composition, lipid rafts, and the ordered positioning of membrane proteins all make possible the membrane potentials[39] that govern phenomena ranging from cell shape and division, polar nutrient and waste transport, and the chemical energy acquired through oxidative phosphorylation and photosynthesis. Contemporary cell membranes are heavily and asymmetrically decorated with proteins to manage all these diverse membrane functions.[40]

The discovery of peptide membranes with a well-ordered charged lattice defining the leaflet interface[11,13] (Figure S1) suggests that patterned electrostatic complementarity can be used to spontaneously assemble bilayer asymmetry. Coassembly of peptide monomers carrying opposite charges, like single peptide assemblies,[16] form intermediate particles with mixed electrostatic surfaces. Nucleation of paracrystalline phases form later, consistent with numerous computational models[41−43] and experimental studies,[44−46] highlighting the importance of

electrochemical interactions in nucleation.[36,37] The methods reported here not only define the electrochemical composition of the supramolecular surfaces but also enable imaging the diverse bamboo-like segments that form along the nanotube axis. Site-specific isotopic enrichments define the population differences in each architectural arrangement and allow for atomic-level structural assignments, but additional experimental constraints are still needed for full structural characterization.

On the basis of the seeding experiments reported here (Figure 8), the K and pY peptides are able to template growth of oppositely charged peptides. Segmentation domains within nanotubes have been observed with fluorescent lifetime measurements[35] and have been proposed as the source of "propagation mutations" that arise during the extension of fiber assemblies.[36,37] The precise propagation mutation rates are not yet known, but the K/pY peptide coassemblies suggest that such structural changes are sufficiently frequent that transition zones are not resolved by TEM. The rates of propagation, conformational mutation, and most importantly, particle association dynamics with the active seed ends,[16] are all expected to be context-dependent. It should now be possible to identify conditions where fine control over nanotube lateral architecture can be achieved.

Therefore, the robust bilayer scaffold afforded by simple peptides carrying high cross-β propensity opens various new opportunities for constructing functional mesoscale materials.[47−50] These coassemblies are distinct from previously studied membranes in many respects. First, the ordered cross-β nanotube structures are controlled largely by lattice electrochemical passification at the leaflet lattice interface. Second, the solvent-exposed lattices are dense and oppositely charged on the inner and outer surfaces of the nanotube, constituting to our knowledge the first example of such significant charge separation in membrane assembly. Third, peptide registry contains both homogeneous and heterogeneous leaflet interfaces that have distinct properties and rates of assembly that appear to be controllable. And finally, asymmetry can be controlled not only across the peptide bilayer but also along the lateral axis of the nanotube membranes. These new mesoscale architectures suggest that asymmetric peptide membranes can serve as scaffolds for mesoscale ordering of electrically and optically functional materials,[35,48] as templates for ordering substrate molecules,[18] metals[50,51] and even large proteins,[13] and as building blocks for even high-order organic frameworks and functional machines.

MATERIALS AND METHODS

Peptide Synthesis and Purification. Peptides were synthesized using a Liberty CEM Microwave Automated Peptide Synthesizer (Matthews, NC, USA) using standard solid-phase peptide synthesis protocols with FMOC-Rink Amide MBHA Resin (AnaSpec, Fremont, CA, USA). Briefly: microwave assisted FMOC deprotection was accomplished with 20% piperidine in dimethylformamide (DMF) at 45−55 °C for 180 s. Each amino acid coupling step used 0.1 M FMOC protected amino acid, activated with 0.1 M 2-(1H-benzotriazol-1-yl)-1,1,3,3-tetramethyluronium hexafluorophosphate (HBTU), and 0.2 M N,N-diisopropylethylamine (DIEA) in DMF. Coupling temperatures were maintained between 75 and 82 °C for 300 s. Phosphotyrosine was double coupled with a final temperature for coupling of 75 °C. Acetylation of the N-terminus was achieved by addition 20% acetic anhydride in DMF. Peptides were cleaved from resin using trifluoroacetic acid/thioanisole/1,2-ethanedithiol/anisole (90:5:3:2, v/v/v/v) at room temperature for 3 h and precipitated by dropwise addition to cold (−20 °C) diethyl ether. Ac-KLVFFAL-NH₂ peptide

was purified by RP-HPLC using C18-reverse phase chromotrography with an acetonitrile−water+0.1% TFA gradient. Ac-(pY)LVFFAL-NH$_2$ peptide was purified by RP-HPLC with an acetonitrile-triethylamounium acetate buffer (pH 7) gradient. Molecular weight was confirmed by MALDI-TOF using a 2,5-dihydroxybenzoic acid matrix.

Peptide Coassembly. Ac-KLVFFAL-NH$_2$ and Ac-(pY)LVFFAL-NH$_2$ peptide powders are mixed in equal ratios, suspended and dried from hexafluoroisopropanol (HFIP) to remove preformed structures, and dissolved as a 1:1 molar ratio in 40%MeCN/H$_2$O adjusted to pH 7 with NaOH for assembly. Total peptide concentration is set at 1 mM unless otherwise stated.

TEM. Peptide suspensions are adsorbed on TEM carbon grids for 1 min and excess solution is wicked away with filter paper tips. Uranyl acetate (2-wt %) is added and incubated for 3−5 min before the solution is wicked away with filter paper tips and the grids placed in a vacuum desiccator overnight. TEM micrographs were acquired using a Philips 410 TEM at magnifications ranging from 7100× to 69 000× with a Tungsten filament at an accelerating voltage of 75 kV. Width measurements were obtained from TEM images and diameters estimated as the measured width × 2/π.

Bundling Peptide Nanotubes. Salts are added in a 4.5:1 molar excess to peptide assemblies to induce bundling. The white precipitate that forms, usually within several minutes, is pelleted at 13 000g for 10 min, and resuspended in the same solvent as assembly for addition to TEM grids. If no precipitant forms after 1 h, the initial solution is used for TEM analyses directly. White precipitant clearly form when SO$_4^{2-}$ is added to K nanotubes and Mg^{2+} is added to pY and K/pY nanotubes.

Electrostatic Force Microscopy. Electrostatic force microscopy (EFM) is performed with Park System XE-100 AFM. Ten μL of the peptide nanotubes suspended in the assembly solvent are placed on Si/SiO$_2$ substrates with an oxide layer thickness of 300 nm and air-dried for 12 h. Pt−Ir coated electrically conductive cantilevers with a tip radius <20 nm and a force constant 2.8 N/m are used to map electrochemical properties of the samples at ambient temperatures.

Apart from the electrostatic force, van der Waals forces between the tip and the sample surface are always present.[51] The magnitude of the van der Waals forces changes according to the tip−sample distance, and are used to measure the surface topography. Hence, the obtained signal contains both information on surface topography ("Topo signal") and information on surface electrical properties ("EFM signal").[51,52] Enhanced EFM (Ext)[53] is used to separate the EFM signal from the entire signal.

Atomic Force Microscopy. 20 μL of assembled peptide solutions are diluted to desired concentration and placed on a silicon chip (4″ diameter diced silicon wafer (TedPella, Inc., Redding, CA) previously cleaned by sonication in methanol for 20 min) for 1 min at room temperature. Excess solution is removed by wicking with filter paper and the chip was rinsed with distilled H$_2$O. Tapping mode analysis on a JEOL JSPM-4210 scanning probe microscope employed ultrasharp noncontact silicon cantilevers (MikroMasch, Wilsonville, OR) with typical frequencies between 240 and 350 kHz. Images are collected for dry samples.

Confocal Imaging. Mature assemblies (1 mM) are diluted 10 times, mixed in a 500:1 concentration ratio with Alexa 633 or acridine orange, and loaded onto a 22 × 50 mm #1.5 coverslip in a custom designed holder and enclosed with a 22 × 30 mm coverslip. Fluorescence images are taken on an Olympus Fluoview FV1000 Confocal Microscope using an Olympus 60× oil immersion (PlanApo N, 1.42 NA) objective lens. Each fluorescence intensity acquisition consisted of one frame at 1024 × 1024 pixels with dimensions 212 × 212 μm, 106 × 106 μm or 70 × 70 μm and the images are acquired approximately 2−5 μm below the glass surface. The image data are analyzed by Olympus Fluoview and FIJI.

Solid-State NMR. Prior to assembly, a 1:1 pY:K peptide ratio was confirmed by HPLC. To prepare samples for solid-state NMR, lateral bundling of nanotubes is accomplished by addition of, sodium sulfate or magnesium chloride to Ac-KLVFFAL-NH$_2$, Ac-(pY)LVFFAL-NH$_2$, or the Ac-KLVFFA-NH$_2$ and Ac-(pY)LVFFAL-NH$_2$ coassemblies to a final ratio of peptide to salt of 1:5. Previously, sulfate bundling of

nanotubes has been shown to protect assemblies from freezing and lyophilization.[17] The resulting white precipitate is pelleted by centrifugation for 10 min at 13000g to remove any unassembled peptides, frozen and lyophilized to yield dry powder. TEM confirmed the presence of only intact tubes after lyophilization. The NMR sample (~40 mg) is packed into a 4 mm solid-state NMR rotor and centered using boron nitride spacers.

The relative ratio of pY to K peptide was measured with a ^{13}C spin−echo collected with a Bruker (Billerica, MA, USA) Avance III 300 spectrometer and Bruker 4 mm HCN biosolids magic-angle spinning (MAS) probe. The rotor-synchronized 4 μs ^{13}C (75.475 MHz) refocusing pulse followed EXORCYCLE phase cycling[19,20] with 100 kHz SPINAL64[54] ^{1}H (300.132 MHz) decoupling and MAS spin of 12.5 kHz. The repetition delay was set to 5 times the ^{13}C T$_1$ (12s) of the carbonyl carbon. K/pY peptide ratio was determined from integration of the ^{13}CO/^{13}CH$_3$ center band and attendant sidebands (Figure S8).

Rotational-echo double-resonance (REDOR)[31,32] spectra were collected on a Avance 600 spectrometer with an HCN biosolids probe. The pulse sequence for ^{13}C{^{15}N}REDOR consists of two parts, an S sequence that contains both ^{13}C (150.928 MHz) and ^{15}N (60.818 MHz) rotor synchronized π-pulses, and the S$_0$ sequence which is identical but does not contain any ^{15}N dephasing pulses. xy8-REDOR with half of the π-pulses on the observe spin ^{13}C channel and other half on the dephasing spin[55] ^{15}N channel is used to maximize the observed ^{13}C T$_2$. RF excitation of the dephasing ^{15}N spins interferes with the averaging of the ^{13}C−^{15}N dipolar coupling due to magic-angle spinning and is observed in the REDOR S spectrum, where the signal decays according to both T$_2$ (spin−spin relaxation) and the heteronuclear ^{13}C−^{15}N dipolar coupling. Maximum dephasing occurs when the spacing between the π-pulses is equal to 1/2 of the rotor-cycle. The sequence without any ^{15}N dephasing π-pulses gives the REDOR full-echo or S$_0$ spectra, where the magnetization decays according to only T$_2$. The difference between the REDOR S and S$_0$ signal (ΔS) is directly proportional to the dipolar coupling, hence the distance between the two spins.

To compensate for pulse imperfections, xy8 phase cycling[56] of ^{13}C{^{15}N}REDOR 4 and 8 μs rotor-synchronized ^{13}C and ^{15}N π-pulses, respectively, and EXORCYCLE phase cycling[19,20] of the final ^{13}C Hahn-echo refocusing pulse is applied with 128 kHz Spinal64[54] ^{1}H (600.133 MHz) decoupling. To minimize the effects of RF inhomogeneity,[20,22] ^{13}C π-pulse power level is arrayed in the REDOR S$_0$ pulse sequence at a REDOR evolution time of 54.4 ms (corresponding to ~544 4 s ^{13}C π pulses) and choosing the power level that corresponded to maximum signal intensity.[15] Similarly, ^{15}N π-pulses are optimized by arraying the ^{15}N power level using the REDOR S experiment at REDOR evolution times corresponding to a $\Delta S/S_0$ between 0.3 and 0.5.[15] REDOR data points are the integrated sum of center- and sideband peaks. Error bars are calculated using the noise of each spectrum as the maximum peak height deviation. To normalize for the decay due to T$_2$ (spin−spin relaxation), individual REDOR curves are plotted as $\Delta S/S_0$. The steepness the slope of the REDOR dephasing curves is directly related to the ^{13}C−^{15}N dipolar coupling, hence the distance between the spins. When more than one ^{15}N is present, the resulting ^{13}C{^{15}N}REDOR curve depends on both the ^{13}C−^{15}N distances as well as the relative orientations of the ^{13}C−^{15}N internuclear vectors.[57,58]

By plotting REDOR as $\Delta S/S_0$, the plateau (max dephasing) is directly related to the number of spins that are coupled. For example, if only half of the observe spins (in this case ^{13}C) are coupled to a dephasing spin (in this case ^{15}N), the REDOR curve will achieve half the value observed when all the spins are coupled. In dephasing the carbonyl carbon of Ac-KLVFF [1-^{13}C]AL-NH$_2$ in Ac-pYL [^{15}N]VFF [3-^{13}C]AL-NH$_2$ coassemblies, the distance of the H-bonded ^{15}N from the adjacent peptide was set to 4.32 Å (r_1) and the distance to the non-H-bonded ^{15}N was set to 5.3 Å (r_2). The angle between the two ^{13}C−^{15}N internuclear vectors was set to 155°, consistent with dephasing of Ac-KL[^{13}C]VFF [^{15}N]AL-NH$_2$ self-assemblies. The experimental data was fit to a linear combination of 3-spin (one ^{13}C

and two ^{15}N's) and ^{13}C{^{15}N}REDOR curves corresponding to the ^{13}C–^{15}N distances sufficient to fit the experimental data points using the Nonlinear Fit routine in Mathematica. Individual curves for dephasing of the carbonyl carbon of Ac-KLVFF [1-^{13}C]AL-NH$_2$ and Ac-pYL [^{15}N]VFF [3-^{13}C]AL-NH$_2$ is shown in Figures 6 and 7.

Seeding. Ac-KLVFFAL-NH$_2$, Ac-(pY)LVFFAL-NH$_2$ and a 1:1 molar mixture of these peptides are allowed to assemble into mature nanotubes. Seeds are prepared by sonication of 0.5−1 mL of 1 mM peptide assemblies in 1.5 mL plastic vials in a Branson 3510 sonication bath at high power for 3 h. The resulting seeds were added to HFIP pretreated peptide solutions at a molar seed/peptide ratio of 1:9 unless otherwise specified.

■ ASSOCIATED CONTENT

Ⓢ Supporting Information

The Supporting Information is available free of charge on the ACS Publications website at DOI: 10.1021/jacs.6b00977.

CD, IR, XRD, melting, EFM and confocal microscopy of peptide coassemblies and ^{13}C{^{15}N}REDOR of pure peptide assemblies. (PDF)

■ AUTHOR INFORMATION

Corresponding Authors
*anil.mehta@emory.edu
*david.lynn@emory.edu

Notes
The authors declare no competing financial interest.

■ ACKNOWLEDGMENTS

■ REFERENCES

(1) Niece, K. L.; Hartgerink, J. D.; Donners, J. J. J. M.; Stupp, S. I. *J. Am. Chem. Soc.* **2003**, *125*, 7146.
(2) Behanna, H. A.; Donners, J. J. J. M.; Gordon, A. C.; Stupp, S. I. *J. Am. Chem. Soc.* **2005**, *127*, 1193.
(3) Ramachandran, S.; Flynn, P.; Tseng, Y.; Yu, Y. B. *Chem. Mater.* **2005**, *17*, 6583.
(4) Ramachandran, S.; Taraban, M. B.; Trewhella, J.; Gryczynski, I.; Gryczynski, Z.; Yu, Y. B. *Biomacromolecules* **2010**, *11*, 1502.
(5) Xu, X.-D.; Chen, C.-S.; Lu, B.; Cheng, S.-X.; Zhang, X.-Z.; Zhuo, R.-X. *J. Phys. Chem. B* **2010**, *114*, 2365.
(6) Madine, J.; Davies, H. A.; Shaw, C.; Hamley, I. W.; Middleton, D. A. *Chem. Commun. (Cambridge, U. K.)* **2012**, *48*, 2976.
(7) Morris, K. L.; Zibaee, S.; Chen, L.; Goedert, M.; Sikorski, P.; Serpell, L. C. *Angew. Chem., Int. Ed.* **2013**, *52*, 2279.
(8) Childers, W. S.; Mehta, A. K.; Ni, R.; Taylor, J. V.; Lynn, D. G. *Angew. Chem., Int. Ed.* **2010**, *49*, 4104.
(9) Inouye, H.; Fraser, P. E.; Kirschner, D. A. *Biophys. J.* **1993**, *64*, 502.
(10) Sunde, M.; Blake, C. C. *Q. Rev. Biophys.* **1998**, *31*, 1.
(11) Mehta, A. K.; Lu, K.; Childers, W. S.; Liang, Y.; Dublin, S. N.; Dong, J.; Snyder, J. P.; Pingali, S. V.; Thiyagarajan, P.; Lynn, D. G. *J. Am. Chem. Soc.* **2008**, *130*, 9829.
(12) Lu, K.; Jacob, J.; Thiyagarajan, P.; Conticello, V. P.; Lynn, D. G. *J. Am. Chem. Soc.* **2003**, *125*, 6391.
(13) Li, S.; Sidorov, A. N.; Mehta, A. K.; Bisignano, A. J.; Das, D.; Childers, W. S.; Schuler, E.; Jiang, Z.; Orlando, T. M.; Berland, K.; Lynn, D. G. *Biochemistry* **2014**, *53*, 4225.
(14) Guo, Q.; Mehta, A. K.; Grover, M. A.; Chen, W.; Lynn, D. G.; Chen, Z. *Appl. Phys. Lett.* **2014**, *104*, 211102.
(15) Ni, R.; Childers, W. S.; Hardcastle, K. I.; Mehta, A. K.; Lynn, D. G. *Angew. Chem., Int. Ed.* **2012**, *51*, 6635.
(16) Childers, W. S.; Anthony, N. R.; Mehta, A. K.; Berland, K. M.; Lynn, D. G. *Langmuir* **2012**, *28*, 6386.
(17) Lu, K.; Guo, L.; Mehta, A. K.; Childers, W. S.; Dublin, S. N.; Skanthakumar, S.; Conticello, V. P.; Thiyagarajan, P.; Apkarian, R. P.; Lynn, D. G. *Chem. Commun.* **2007**, 2729.
(18) Childers, W. S.; Mehta, A. K.; Lu, K.; Lynn, D. G. *J. Am. Chem. Soc.* **2009**, *131*, 10165.
(19) Miyazawa, T. *J. Chem. Phys.* **1960**, *32*, 1647.
(20) Chirgadze, Y. N.; Nevskaya, N. A. *Biopolymers* **1976**, *15*, 607.
(21) Krimm, S.; Bandekar, J. *Adv. Protein Chem.* **1986**, *38*, 181.
(22) Moran, S. D.; Zanni, M. T. *J. Phys. Chem. Lett.* **2014**, *5*, 1984.
(23) Astbury, W. T.; Dickinson, S.; Bailey, K. *Biochem. J.* **1935**, *29*, 2351.
(24) Parker, K. D.; Rudall, K. M. *Nature* **1957**, *179*, 905.
(25) Eanes, E. D.; Glenner, G. G. *J. Histochem. Cytochem.* **1968**, *16*, 673.
(26) Geddes, A. J.; P, K. D.; Atkins, E. D. T.; Beighton, E. *J. Mol. Biol.* **1968**, *32*, 343.
(27) Gomez, A.; Avila, A.; Hinestroza, J. P. *J. Electrost.* **2010**, *68*, 79.
(28) Clausen, C. H.; Dimaki, M.; Panagos, S. P.; Kasotakis, E.; Mitraki, A.; Svendsen, W. E.; Castillo-Leon, J. *Scanning* **2011**, *33*, 201.
(29) Bonilla, R.; Avila, A.; Montenegro, C.; Hinestroza, J. *J. Microsc.* **2012**, *248*, 266.
(30) Lee, G.; Lee, W.; Lee, H.; Lee, S. W.; Yoon, D. S.; Eom, K.; Kwon, T. *Appl. Phys. Lett.* **2012**, *101*, 043703.
(31) Gullion, T.; Schaefer, J. *J. Magn. Reson.* **1989**, *81*, 196.
(32) Gullion, T.; Schaefer, J. *Adv. Magn. Opt. Reson.* **1989**, *13*, 57.
(33) Wishart, D. S.; Sykes, B. D.; Richards, F. M. *J. Mol. Biol.* **1991**, *222*, 311.
(34) Balbach, J. J.; Ishii, Y.; Antzutkin, O. N.; Leapman, R. D.; Rizzo, N. W.; Dyda, F.; Reed, J.; Tycko, R. *Biochemistry* **2000**, *39*, 13748.
(35) Anthony, N. R.; Mehta, A. K.; Lynn, D. G.; Berland, K. M. *Soft Matter* **2014**, *10*, 4162.
(36) Liang, C.; Ni, R.; Smith, J. E.; Childers, W. S.; Mehta, A. K.; Lynn, D. G. *J. Am. Chem. Soc.* **2014**, *136*, 15146.
(37) Smith, J. E.; Liang, C.; Tseng, M.; Li, N.; Li, S.; Mowles, A. K.; Mehta, A. K.; Lynn, D. G. *Isr. J. Chem.* **2015**, *55*, 763.
(38) Nicolson, G. L. *Biochim. Biophys. Acta, Biomembr.* **2014**, *1838*, 1451.
(39) Gurtovenko, A. A.; Vattulainen, I. *J. Am. Chem. Soc.* **2007**, *129*, 5358.
(40) Cooper, G. M. *The Cell—A Molecular Approach*, 2nd ed.; Sinauer Associates: Sunderland, MA, 2000.
(41) Yun, S.; Urbanc, B.; Cruz, L.; Bitan, G.; Teplow, D. B.; Stanley, H. E. *Biophys. J.* **2007**, *92*, 4064.
(42) Buell, A. K.; Hung, P.; Salvatella, X.; Welland, M. E.; Dobson, C. M.; Knowles, T. P. *J. Biophys. J.* **2013**, *104*, 1116.
(43) Tarus, B.; Straub, J. E.; Thirumalai, D. *J. Mol. Biol.* **2005**, *345*, 1141.
(44) Konno, T. *Biochemistry* **2001**, *40*, 2148.
(45) Raman, B.; Chatani, E.; Kihara, M.; Ban, T.; Sakai, M.; Hasegawa, K.; Naiki, H.; Rao, C. M.; Goto, Y. *Biochemistry* **2005**, *44*, 1288.
(46) Shammas, S. L.; Knowles, T. P. J.; Baldwin, A. J.; MacPhee, C. E.; Welland, M. E.; Dobson, C. M.; Devlin, G. L. *Biophys. J.* **2011**, *100*, 2783.
(47) Kapil, N.; Singh, A.; Das, D. *Angew. Chem., Int. Ed.* **2015**, *54*, 6492.

(48) Dai, B.; Li, D.; Xi, W.; Luo, F.; Zhang, X.; Zou, M.; Cao, M.; Hu, J.; Wang, W.; Wei, G.; Zhang, Y.; Liu, C. *Proc. Natl. Acad. Sci. U. S. A.* **2015**, *112*, 2996.

(49) Ni, R.; Chau, Y. *J. Am. Chem. Soc.* **2014**, *136*, 17902.

(50) Webber, M. J.; Appel, E. A.; Meijer, E. W.; Langer, R. *Nat. Mater.* **2016**, *15*, 13.

(51) Butt, H.-J. *Biophys. J.* **1991**, *60*, 1438.

(52) Digital Instruments, http://nanopicolab.cnsi.ucla.edu/pages/publicview/manuals/230A-EFM.pdf, 1996.

(53) Park Systems, http://www.parkAFM.com, accessed 01/25/2016.

(54) Fung, B. M.; Khitrin, A. K.; Ermolaev, K. *J. Magn. Reson.* **2000**, *142*, 97.

(55) Christensen, A. M.; Schaefer, J. *Biochemistry* **1993**, *32*, 2868.

(56) Gullion, T.; Baker, D. B.; Conradi, M. S. *J. Magn. Reson.* **1990**, *89*, 479.

(57) Jarvie, T. P.; Went, G. T.; Mueller, K. T. *J. Am. Chem. Soc.* **1996**, *118*, 5330.

(58) Goetz, J. M.; Schaefer, J. *J. Magn. Reson.* **1997**, *127*, 147.